

Temporal and spatial variabilities of the South China Sea surface temperature anomaly

Peter C. Chu, Shihua Lu,¹ and Yuchun Chen¹

Department of Oceanography, Naval Postgraduate School, Monterey, California

Abstract. In this study we use the National Centers for Environmental Prediction (NCEP) monthly sea surface temperature (SST) fields (1982-1994) to investigate the temporal and spatial variabilities of the South China Sea (SCS) warm/cool anomalies. Three steps of analysis were performed on the data set: ensemble mean (\overline{T}), composite analysis to obtain the monthly mean anomaly relative to the ensemble mean (\overline{T}), and empirical orthogonal function (EOF) analysis on the residue data relative to $\overline{T} + \tilde{T}$. The ensemble mean SST field (\overline{T}) has a rather weak horizontal gradient: 29°C near the Borneo coast to 25°-26°C near the southeast China coast. Two areas of evident SST anomalies were found in the monthly \tilde{T} variation: west of Borneo-Palawan Islands (WBP) and southeast of the southern Vietnam coast (SVC). Four patterns, monsoon and transition each with two out-of-phase structures, were found. During the spring-to-summer transition (March to May) the warm anomaly is formed in the northern SCS with $\tilde{T} > 1.8^\circ\text{C}$ located at 112°-119°30'E, 15°-19°30'N. During the fall-to-winter transition (October to November) the northern SCS (north of 12°N) cool anomaly is formed in November with $\tilde{T} < -0.6^\circ\text{C}$ located at 108°-115°E, 13°-20°N. We performed an EOF analysis on the residue data relative to $\overline{T} + \tilde{T}$ in order to obtain transient and interannual variations of the SST fields. EOF1 accounts for 47% of the variance and represents the northern SCS warm/cool anomaly pattern. EOF2 accounts for 14% of the variance and represents the southern SCS dipole pattern. Strong northern SCS warm anomaly (1°C warmer) appears during October-November 1987 and January-February 1988, and strong northern SCS cool anomaly (1°C cooler) occurs during March 1986 and November 1992. Furthermore, a strong cross correlation between wind stress curl and SST anomalies, computed from the European Centre for Medium-Range Weather Forecast analyzed wind stress data and the NCEP SST data for different lags, shows the existence of an air-sea feedback mechanism in the SCS deep basin.

1. Introduction

The South China Sea (SCS) has a bottom topography (Figure 1) that makes it a unique semienclined ocean basin that is overlaid by a pronounced monsoon surface wind. Extended continental shelves (less than 200 m deep) are found on the northern and the southwestern parts, while steep slopes with almost no shelves are found in the eastern part of SCS. The deepest water is confined to a bowl-type trench. The maximum depth is around 4700 m.

¹On leave from the Institute of Plateau Atmospheric Physics, Academia Sinica, Lanzhou, China.

This paper is not subject to U.S. copyright. Published in 1997 by the American Geophysical Union.

Paper number 97JC00982.

Based on limited data sets, both cool and warm anomalies were detected in SCS. Dale [1956] reported a cool anomaly off the central Vietnamese coast in summer. Nitani [1970] found a cool anomaly located at the northwest of Luzon. Reports from the *South China Sea Institute of Oceanology* [1985] indicate that in the central South China Sea, a warm anomaly appears in both summer and winter but closer to Vietnam in summer at the surface. Recently, a warm anomaly was reported in the central SCS during the late spring season [Chu and Chang, 1995a, b, 1997; Chu et al., 1996, 1997] and a cool anomaly was detected in the central SCS during December 29, 1993 to January 5, 1994 from the analysis of TOPEX/POSEIDON data [Soong et al., 1995]. What are the temporal and spatial variabilities of sea surface temperature (SST) anomaly? We used the National Centers for Environmental Prediction (NCEP) SST data set to investigate these problems.

Report Documentation Page				Form Approved OMB No. 0704-0188	
Public reporting burden for the collection of information is estimated to average 1 hour per response, including the time for reviewing instructions, searching existing data sources, gathering and maintaining the data needed, and completing and reviewing the collection of information. Send comments regarding this burden estimate or any other aspect of this collection of information, including suggestions for reducing this burden, to Washington Headquarters Services, Directorate for Information Operations and Reports, 1215 Jefferson Davis Highway, Suite 1204, Arlington VA 22202-4302. Respondents should be aware that notwithstanding any other provision of law, no person shall be subject to a penalty for failing to comply with a collection of information if it does not display a currently valid OMB control number.					
1. REPORT DATE 15 SEP 1997		2. REPORT TYPE		3. DATES COVERED 00-00-1997 to 00-00-1997	
4. TITLE AND SUBTITLE Temporal and Spatial Variabilities of the South China Sea Surface Temperature Anomaly				5a. CONTRACT NUMBER	
				5b. GRANT NUMBER	
				5c. PROGRAM ELEMENT NUMBER	
6. AUTHOR(S)				5d. PROJECT NUMBER	
				5e. TASK NUMBER	
				5f. WORK UNIT NUMBER	
7. PERFORMING ORGANIZATION NAME(S) AND ADDRESS(ES) Naval Postgraduate School, Department of Oceanography, Monterey, CA, 93943				8. PERFORMING ORGANIZATION REPORT NUMBER	
9. SPONSORING/MONITORING AGENCY NAME(S) AND ADDRESS(ES)				10. SPONSOR/MONITOR'S ACRONYM(S)	
				11. SPONSOR/MONITOR'S REPORT NUMBER(S)	
12. DISTRIBUTION/AVAILABILITY STATEMENT Approved for public release; distribution unlimited					
13. SUPPLEMENTARY NOTES					
14. ABSTRACT					
15. SUBJECT TERMS					
16. SECURITY CLASSIFICATION OF:			17. LIMITATION OF ABSTRACT Same as Report (SAR)	18. NUMBER OF PAGES 19	19a. NAME OF RESPONSIBLE PERSON
a. REPORT unclassified	b. ABSTRACT unclassified	c. THIS PAGE unclassified			

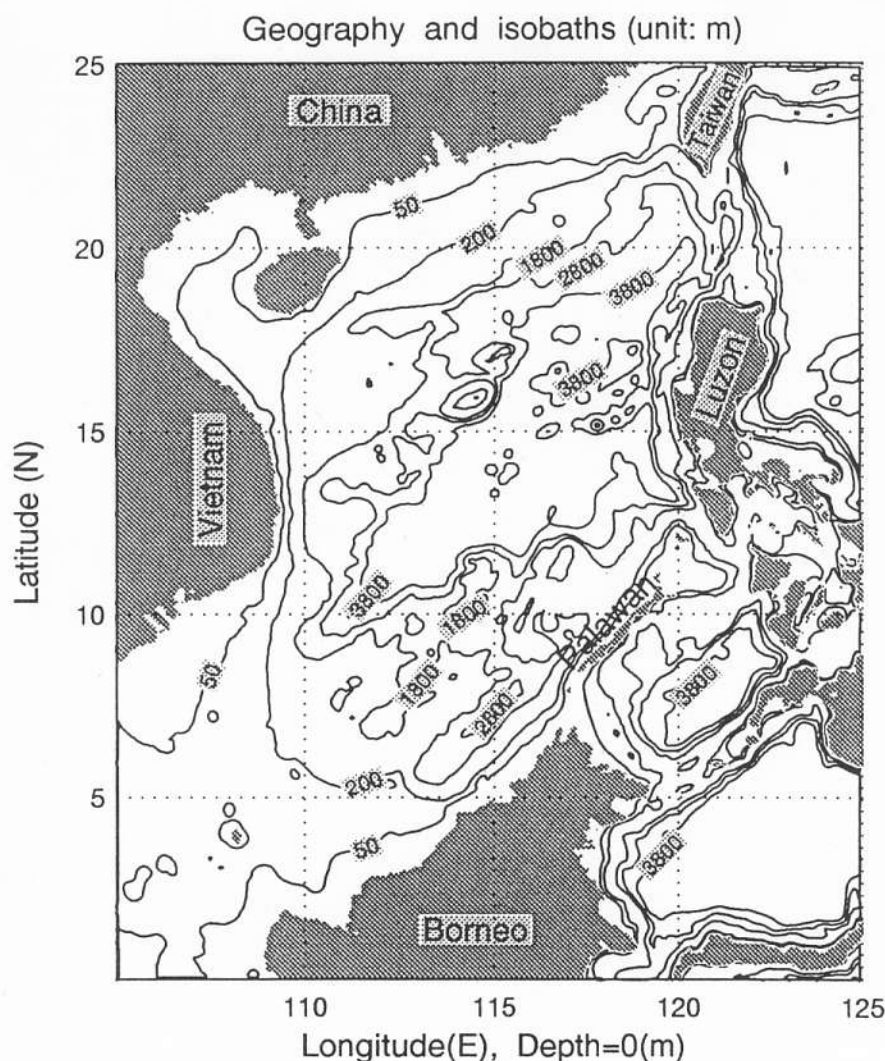


Figure 1. Geography and isobaths showing the bottom topography of the South China Sea.

The SST data (1982-1994) for this study were obtained from the NCEP monthly real-time SST global data set, which was established by blending in situ and satellite SST data [Reynolds, 1988; Reynolds and Marsico, 1993]. The monthly optimum interpolation (OI) fields are derived from linear interpolation of the weekly OI fields to daily fields then averaging the daily values over a month [Reynolds and Marsico, 1993]. The monthly fields have the same spatial resolution ($1^\circ \times 1^\circ$) as the weekly fields. Before the analysis is completed, the satellite data are adjusted for biases using the method of Reynolds [1988] and Reynolds and Marsico [1993]. A description of the OI analysis is given by Reynolds and Smith [1994]. The bias correction improves the large-scale accuracy of the OI. The data processing procedure described here was done by NCEP.

In situ SST data were obtained from the Comprehensive Ocean-Atmosphere Data Set for the period 1981-1989, and from radio message carried on the Global Telecommunication System for the period 1990-present.

The satellite SST data were obtained from analysis of National Environmental Satellite Data and Information Service data by the University of Miami's Rosentiel School of Marine and Atmospheric Sciences. We use the monthly SST for the period 1981-1994 for this study.

2. Seasonal Variation of the SCS Wind Stress

SCS experiences two monsoons, winter and summer, every year. During the winter monsoon season, a cold northeast wind blows over SCS (Figure 2a) as a result of the Siberian high pressure system located over the east Asian continent. Radiative cooling and persistent cold air advection maintain cold air over SCS. The northeast-southwest oriented jet stream is positioned at the central SCS. Such a typical winter monsoon pattern lasts nearly 6 months (November to April). During the summer monsoon season, a warm and weaker southwest wind blows over SCS (Figure 2b). Such a typical sum-

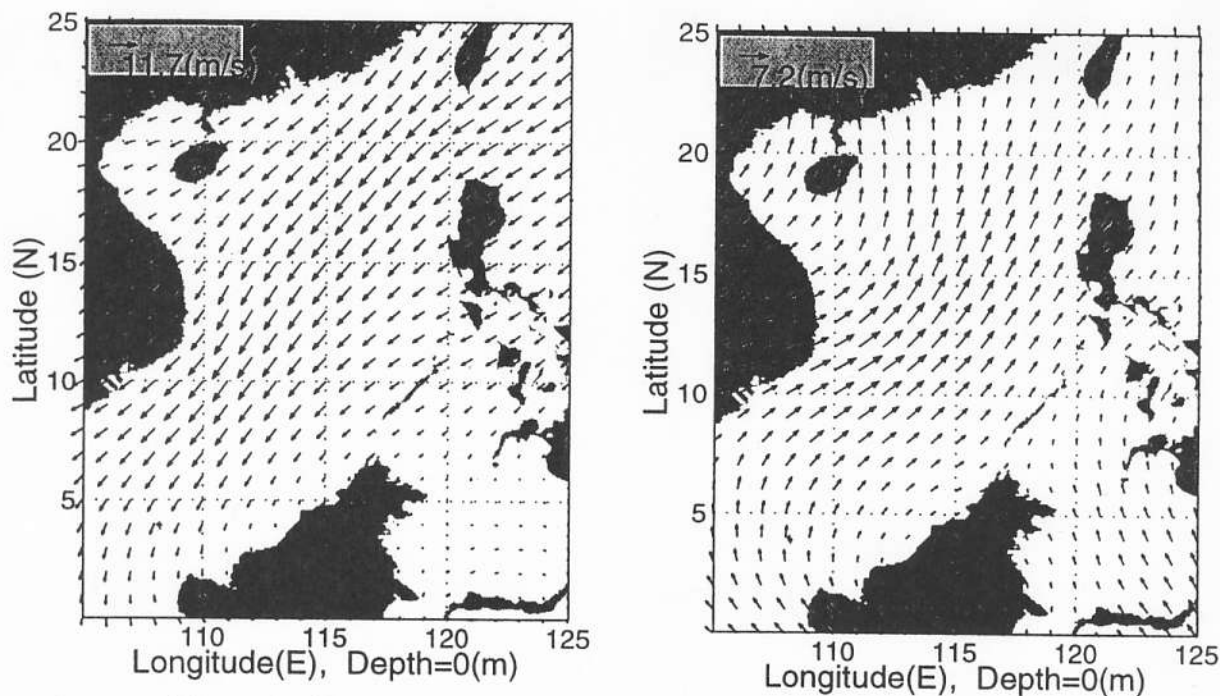


Figure 2. Mean surface wind stress vectors in the South China Sea for (a) December and (b) June (computed from the ECMWF data set).

mer monsoon pattern lasts nearly 4 months (mid-May to mid-September). The mean surface wind stress over SCS is nearly 0.2 N/m^2 and reaches 0.3 N/m^2 in the central portion in December (Figure 2a) and is nearly 0.1 N/m^2 in June (Figure 2b).

Using the European Centre for Medium-Range Weather Forecast (ECMWF) analyzed wind data, Trenberth *et al.* [1989] calculated global monthly mean wind stress curl ζ on a $2.5^\circ \times 2.5^\circ$ grid for the period 1982–1989. The drag coefficient was corrected for atmospheric stability, with sea-air temperature difference and the relative humidity taken to be mean monthly climatological values. The ensemble mean (1982–1989) ζ field (Figure 3a) shows a dipole pattern: cyclonic curls over the eastern SCS and anticyclonic curls over the western SCS. This coincides with the prevailing northeast winds over the central SCS.

Four patterns, monsoon and transition each with two out-of-phase structures, were found (Figures 3b–3e). The monsoon pattern is featured by a northwest anticyclonic (cyclonic) curl and a southeast cyclonic (anticyclonic) curl in winter (summer). The transition pattern is featured by a southern SCS cyclonic/anticyclonic dipole.

1. Fall-to-winter transition pattern shows a southern SCS (south of 12°N) dipole curl structure located at the west of Borneo-Palawan Islands (WBP) and the south-east of the southern Vietnam coast (SVC). The typical pattern is featured by a WBP anticyclonic curl and a SVC cyclonic curl (Figure 3b). The strength of the curl is quite weak, and the maximum absolute value is $1.2 \times 10^{-7} \text{ N/m}^3$ for the cyclonic curl and $0.6 \times 10^{-7} \text{ N/m}^3$ for the anticyclonic curl.

2. Winter monsoon pattern: During the winter monsoon season, a northeast-to-southwest oriented line separates the SCS into two parts: the western part under anticyclonic wind stress curl and the eastern part is under cyclonic wind stress curl, that is, the AC-C pattern (Figure 3c). The maximum absolute values of both curls reach $4 \times 10^{-7} \text{ N/m}^3$. Such a pattern persists from November to March.

3. Spring-to-summer transition pattern shows an opposite dipole pattern to the fall-to-winter transition period. The dipole curl is characterized by a WBP cyclonic curl and a SVC anticyclonic curl (Figure 3d). The strength of the dipole curl is much weaker than the winter monsoon period.

4. Summer monsoon pattern is 180° out-of-phase with the winter monsoon pattern. A northeast-to-southwest oriented line separates the SCS into two parts: the western part under cyclonic wind stress curl and the eastern part is under anticyclonic wind stress curl (Figure 3e). The strength of the wind stress curl during summer monsoon season is about half that during winter monsoon season.

3. Composite Analysis of SST

3.1. Ensemble Mean SST Field

We now examine the data to see if we can obtain a warm anomaly signal. SST is represented by $T(x_i, y_j, \chi_k, t_l)$, where (x_i, y_j) is the horizontal grids, $\chi_k = 1982, 1983, \dots, 1994$ is the time sequence in years, and $t_l = 1, 2, \dots, 12$ is the monthly sequence within a year. Before investigating the monthly variation of SST, we define the following two temporal averages:

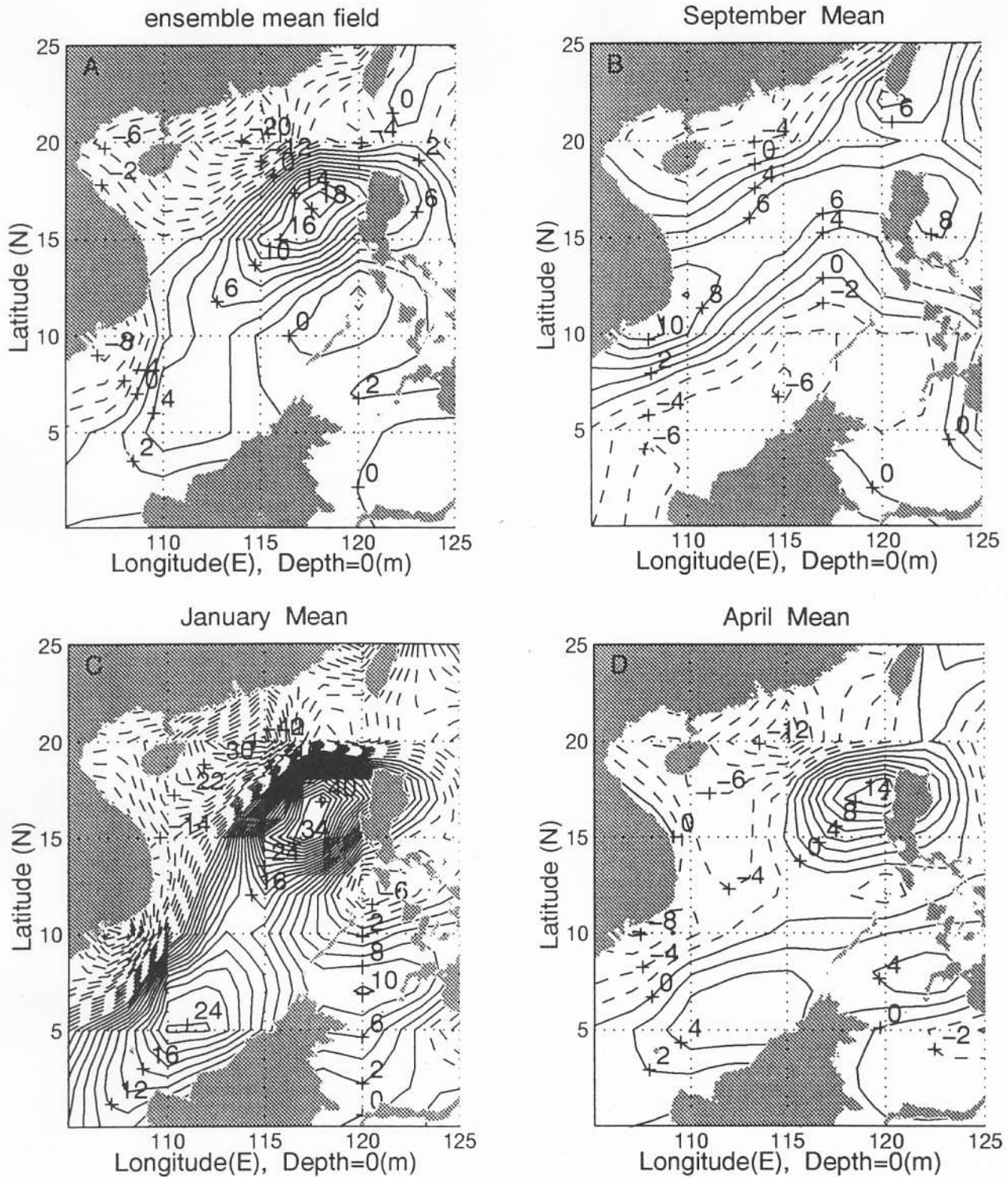


Figure 3. Surface wind stress curl: (a) ensemble mean, (b) September, (c) January, (d) April, and (e) July (computed from Trenberth *et al.* 1989). The unit is 10^{-8} N/m^3 .

$$\bar{T}(x_i, y_j, t_l) \equiv \frac{1}{\Delta\chi} \sum_{k=1982}^{1994} T(x_i, y_j, \chi_k, t_l),$$

$$\Delta\chi \equiv 13 \quad (1994 - 1982 + 1). \quad (1)$$

which is the long-term mean value for the month t_l , and

$$\bar{\bar{T}}(x_i, y_j) \equiv \frac{1}{12} \sum_{l=1}^{12} \bar{T}(x_i, y_j, t_l) \quad (2)$$

which is the ensemble mean. The ensemble mean (1982–1994) SST field over the SCS (Figure 4) shows a pattern of northeast-southwest oriented isotherms with a pos-

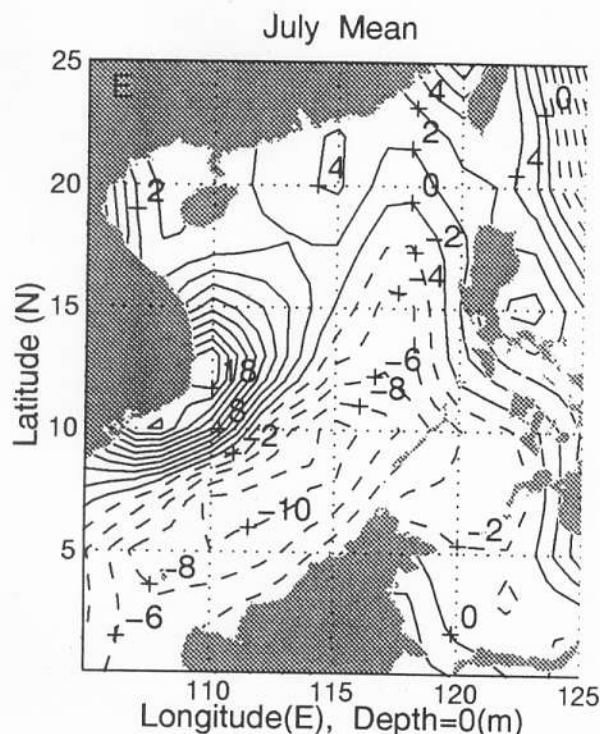


Figure 3. (Continued)

itive temperature gradient toward southeast near the equator. The ensemble mean has a rather weak horizontal temperature gradient, decreasing from 29°C near the Borneo coast to 25°C near the southeast China coast.

3.2. Mean Monthly SST Anomalies (\tilde{T})

The long-term monthly mean values relative to the ensemble mean, $\bar{T}(x_i, y_j)$,

$$\tilde{T}(x_i, y_j, t_l) = \bar{T}(x_i, y_j, t_l) - \bar{T}(x_i, y_j) \quad (3)$$

leads to the composite features of the monthly mean SST anomalies, which have the following features (Figure 5).

1. The typical winter (December to February) \tilde{T} pattern contains northeast-to-southwest oriented isotherms in the northern SCS (north of 12°N), a WBP high anomaly ($\tilde{T} > -1.2^\circ\text{C}$ in January), and a SVC low anomaly ($\tilde{T} < -2.4^\circ\text{C}$ in January) in the southern SCS (south of 12°N).

2. Spring-to-summer transition (March to May) pattern shows the northward expansion of the WBP high anomaly and the formation of a northern SCS (north of 12°N) high anomaly. The isoline of $\tilde{T} = 1^\circ\text{C}$ encloses almost all the SCS in May. The high anomaly with $\tilde{T} > 1.8^\circ\text{C}$ is located at 112°-119°30'E, 15°-19°30'N. A small low anomaly forms near WBP.

3. Summer (June to September) \tilde{T} pattern is characterized by northeast-to-southwest oriented isotherms in the northern SCS (north of 12°N), a WBP low anomaly ($\tilde{T} < 0.4^\circ\text{C}$ in July), and a SVC high anomaly

($\tilde{T} > 1.0^\circ\text{C}$ in July) in the southern SCS. The summer \tilde{T} pattern is out-of-phase of the winter pattern.

4. Fall-to-winter transition (October to November) pattern shows the northward expansion of a WBP low anomaly and the formation of a northern SCS (north of 12°N) low anomaly in November. The low anomaly with $\tilde{T} < -0.6^\circ\text{C}$ is located at 108°-115°E, 13°-20°N (out-of-phase of the spring-to-summer transition pattern). A small high anomaly forms near WBP.

These features can be easily seen from a seasonal mean SST anomaly fields (Figure 6): During winter (December to February) in the north SCS (north of 12°N) isotherms are nearly parallel northeast-southwest oriented curves with \tilde{T} decreasing northward, and in the south SCS (south of 12°N) there exists a WBP high anomaly and a SVC low anomaly (Figure 6a). During spring-to-summer transition, the SVC low anomaly weakens, and the high anomaly (original winter WBP high anomaly) moves toward west, expands northward, and finally forms a large SCS high anomaly. A WBP low anomaly forms (Figure 6b). After \tilde{T} forms the typical pattern shown in Figure 6b, the SCS high anomaly starts to weaken and retreats toward SVC. The north SCS has nearly parallel isotherms with \tilde{T} increases northward, and the WBP low anomaly strengthens. Gradually, it shifts to the summer pattern (Figure 6c), which features a WBP low anomaly and a SVC high anomaly in the south SCS. Such a summer pattern lasts around 4 months (June to September). At the end of summer, the low anomaly (original summer WBP low anomaly) moves westward and expands northward,

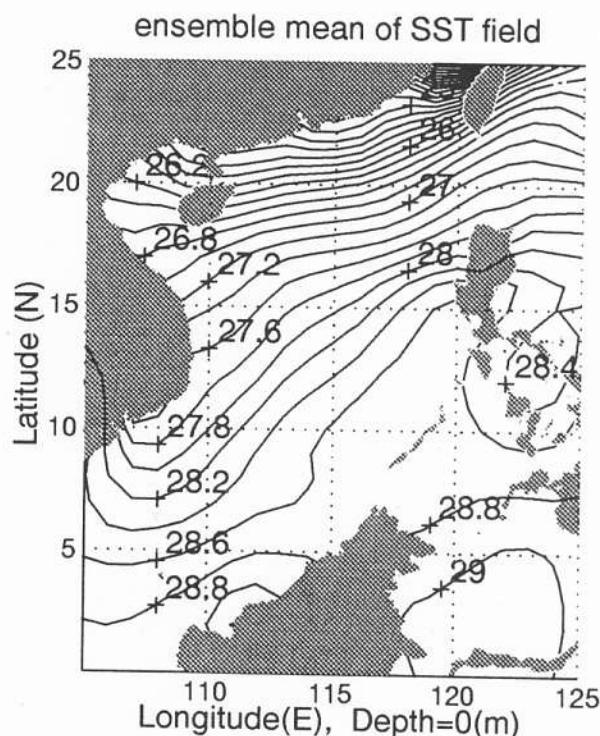


Figure 4. The ensemble mean of the SST field during 1982-94.

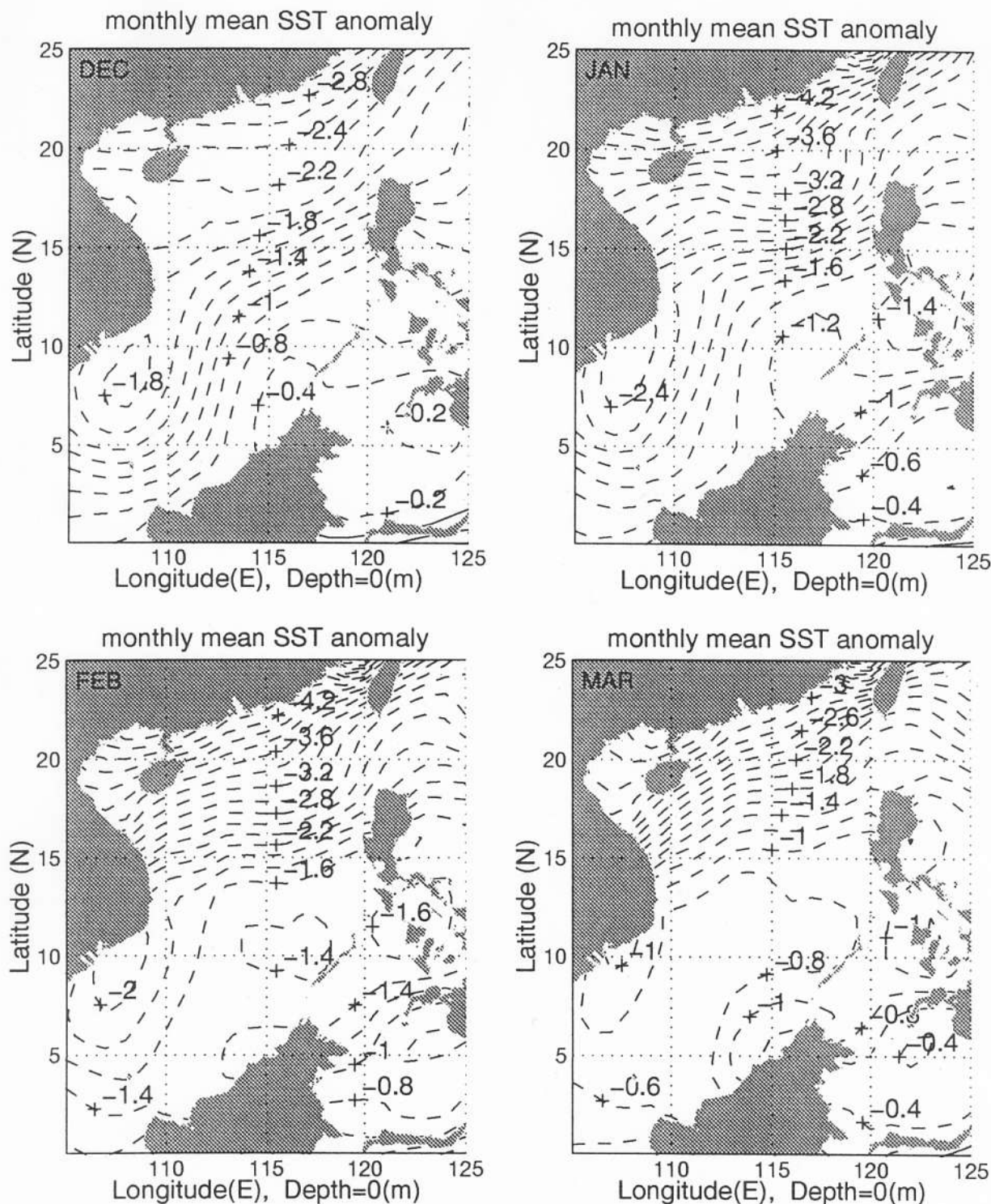


Figure 5. Monthly mean SST anomalies relative to the ensemble mean from the NCEP data set.

forming a large SCS low anomaly. A WBP warm anomaly forms (Figure 6d). After \tilde{T} has the typical pattern shown in Figure 6d, the SCS low anomaly starts to weaken and retreats to SVC. The north SCS has nearly parallel isotherms, and the WBP warm anomaly strengthens. Gradually, it shifts to the winter pattern (Figure 6a).

3.3. Seasonal Phase Shift Between ζ and \tilde{T}

In order to show the phase connection between the mean wind stress curl and the SST anomalies, we purposely put the September (fall) mean ζ as Figure 3b. Comparing Figure 3 to Figure 6, we found some association between the cyclonic (anticyclonic) wind stress

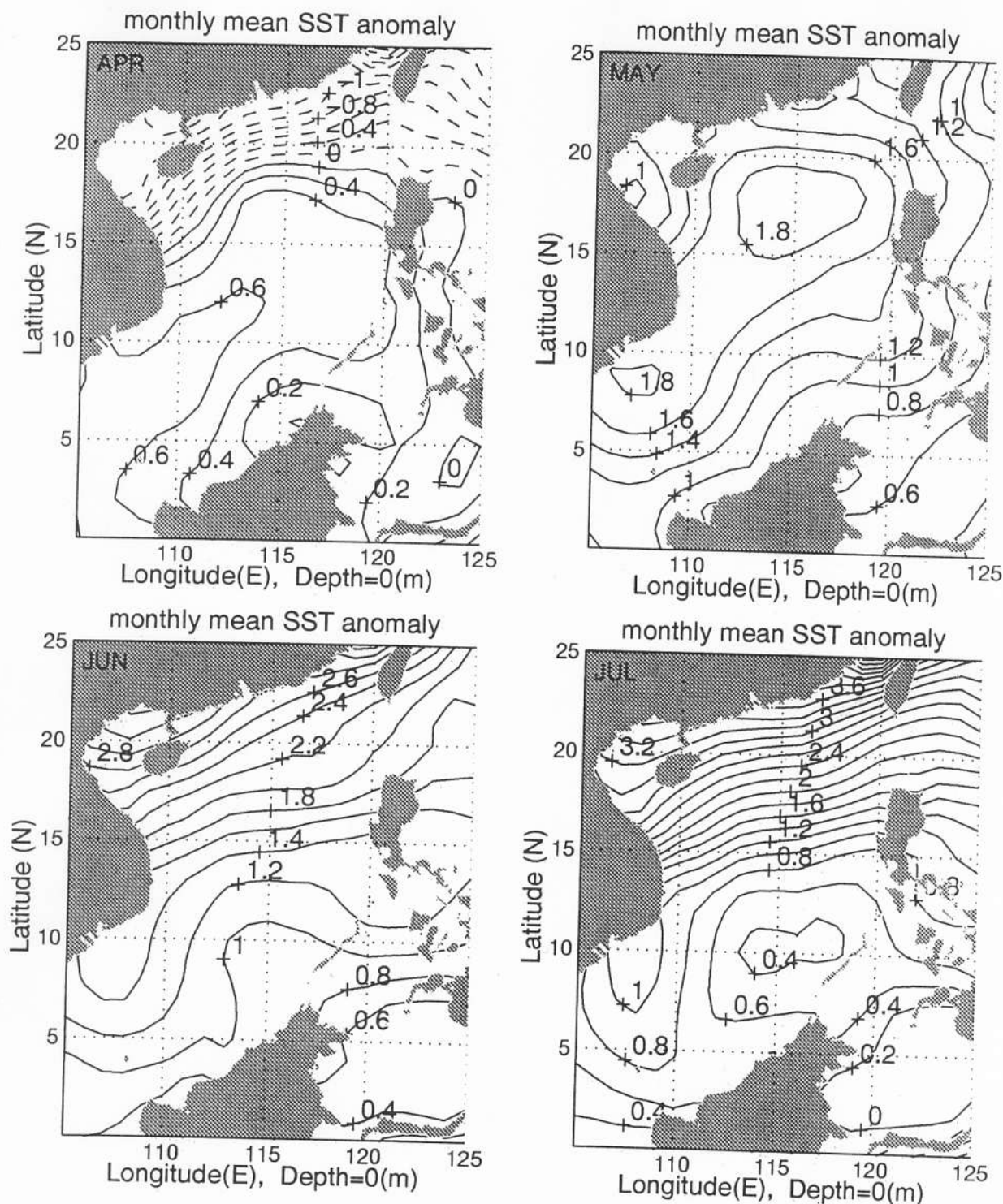


Figure 5. (continued)

curl and the high (low) anomaly with a seasonal phase shift. For the southern SCS, the September (fall) and April (spring) ζ dipole patterns correspond well with the winter and summer \tilde{T} dipole patterns, that is, negative ζ with high \tilde{T} , and positive ζ with low \tilde{T} .

For the central SCS, the winter (summer) ζ pattern corresponds well with the spring (fall) \tilde{T} pattern, that is, the winter negative ζ pattern (Figure 3b) corresponds to the high anomaly pattern in spring (Figure

6b), and the summer positive ζ pattern (Figure 3d) corresponds to the low anomaly pattern in fall (Figure 6d). Thus we may claim that the winter (summer) ζ pattern causes the northward expansion of SVC high (low) anomaly in spring (fall). We will investigate the wind-SST interaction in section 5 by analyzing the cross-correlation coefficients between wind stress curl and SST anomalies.

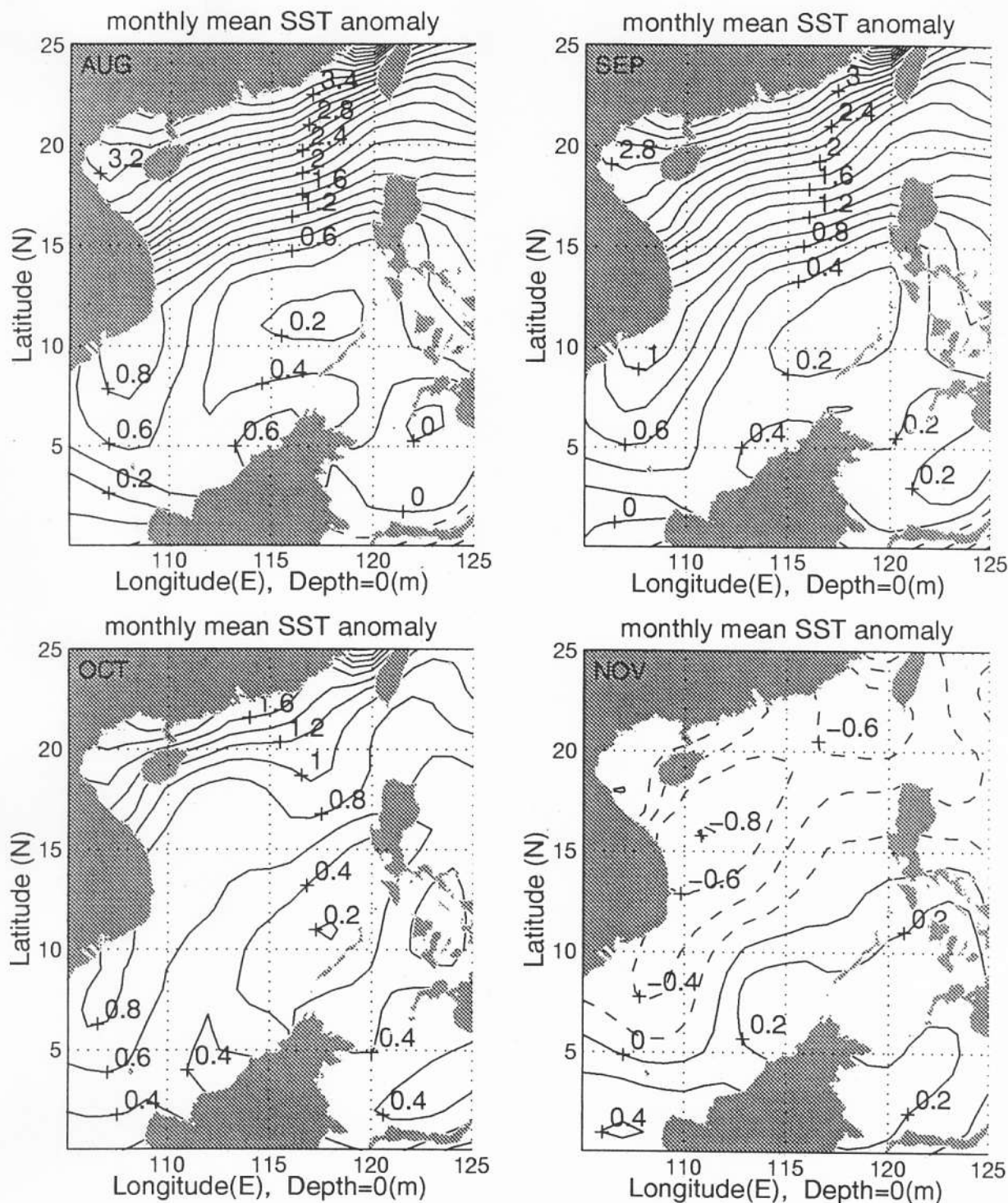


Figure 5. (continued)

4. Empirical Orthogonal Function Analysis of SST

The composite analysis shows the mean seasonal variation of the SST anomaly. Next we use empirical orthogonal function (EOF) analysis to investigate the spatial and temporal variabilities of the SCS high/low anomalies.

4.1. EOFs for the SST Anomalies

The SST synoptic anomalies obtained by

$$\hat{T}(x_i, y_j, \chi_k, t_l) = T(x_i, y_j, \chi_k, t_l) - \bar{T}(x_i, y_j, t_l) \quad (4)$$

are rearranged into a $N \times P$ matrix, $\hat{T}(\mathbf{r}_n, \tilde{t}_p)$, $n = 1, 2, \dots, N$; and $p = 1, 2, \dots, P$. Here $P = 156$ is the total number of time points used for computing the covari-

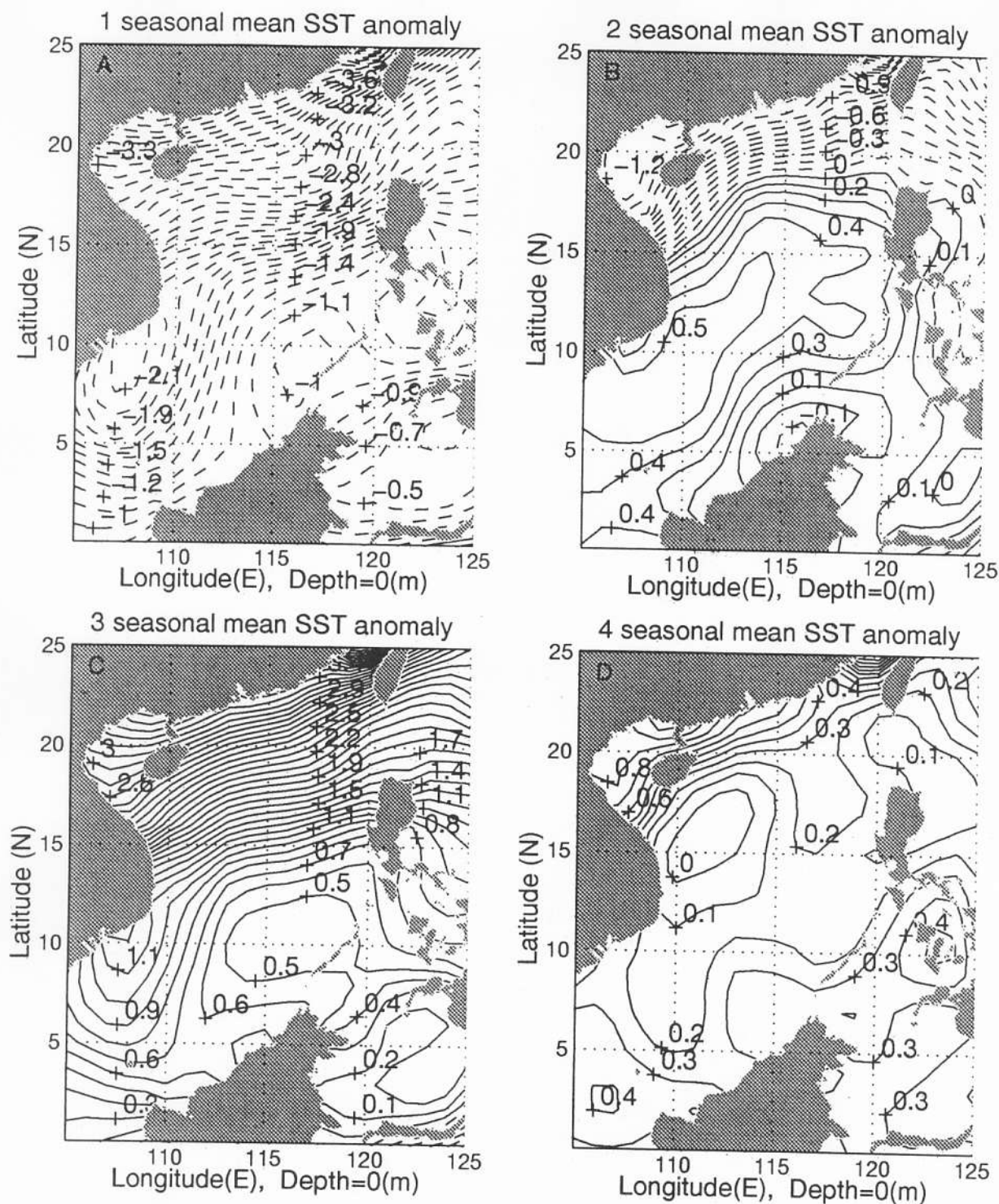


Figure 6. Seasonal mean SST anomaly (relative to ensemble mean) pattern for (a) winter (December to February), (b) spring (March to May), (c) summer (June to September), and (d) fall (October to November).

ance matrix, that is, 13 years of monthly data; $N = 546$ corresponds to the number of grids ($i = 1, 2, \dots, 21; j = 1, 2, \dots, 26$). EOF analysis widely used in oceanographic and meteorological research [e.g., Weare et al., 1976; Richman, 1986] is the same as principal component (PC) analysis [Hotelling, 1933] in the statistics community. PCs are the amplitudes, which are functions of

time, of their corresponding EOFs. These EOFs can be found by calculating the unitary eigenvectors of the covariance matrix associated with the sample data field. EOF analysis separates the data sets into eigenmodes. Generally speaking, each mode has an associated variance, dimensional spatial pattern, and nondimensional time series. From this data matrix a 546-square spatial

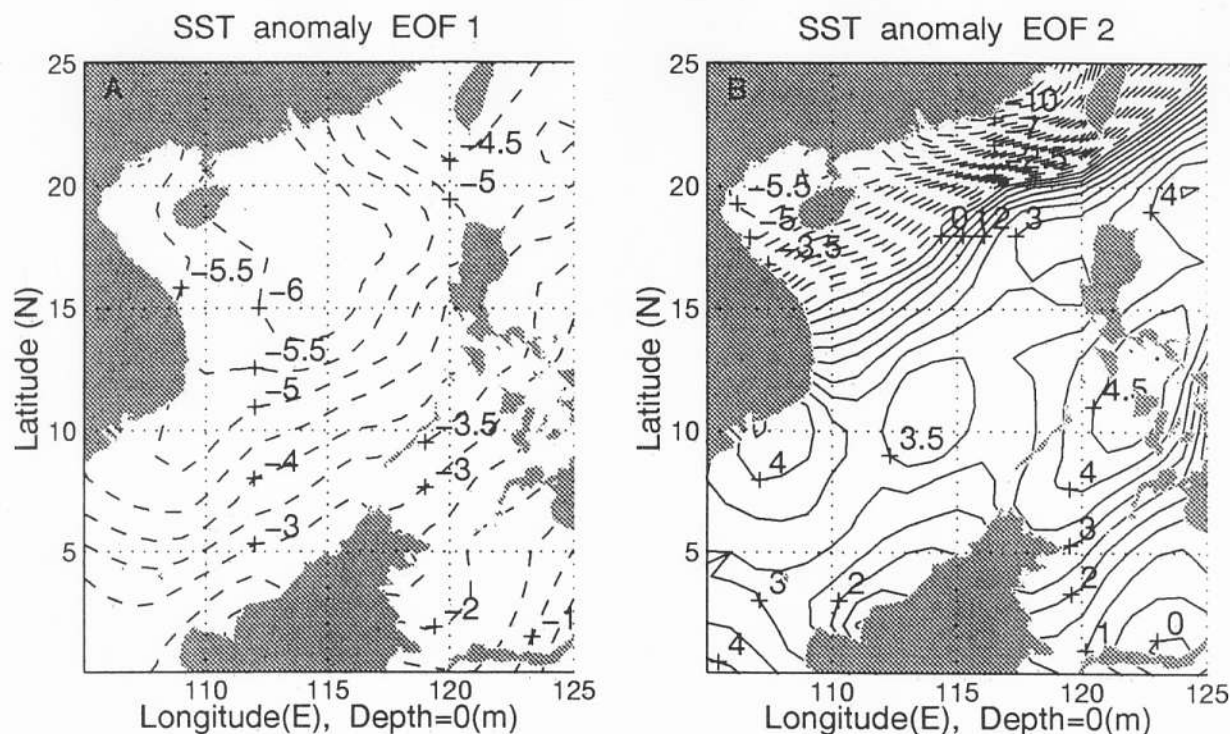


Figure 7. The first two EOF modes (unit 0.01°C): (a) EOF1 and (b) EOF2. The solid (dashed) lines indicate positive (negative) values.

covariance matrix is calculated by

$$R = \begin{bmatrix} R_{11} & R_{12} & \dots & R_{1N} \\ R_{21} & R_{22} & \dots & R_{2N} \\ \dots & \dots & \dots & \dots \\ R_{N1} & R_{N2} & \dots & R_{NN} \end{bmatrix},$$

$$R_{nm} = \sqrt{\frac{1}{P} \sum_p \hat{T}(\mathbf{r}_n, \tilde{t}_p) \hat{T}(\mathbf{r}_m, \tilde{t}_p)}, \quad N = 546, P = 156 \quad (5)$$

where n and m ($1, 2, \dots, N$) denote the grid locations. The diagonal elements of the covariance matrix R_{nn} ($n = 1, 2, \dots, N$) are the variance at location \mathbf{r}_n . The off-diagonal elements are the covariance with spatial lag equal to the difference between the row and column indices. This symmetric matrix has N real eigenvalues λ_α , and eigenvectors $\phi_\alpha(\mathbf{r}_j)$, such that

$$\sum_{j=1}^N R_{ij} \phi_\alpha(\mathbf{r}_j) = \lambda_\alpha \phi_\alpha(\mathbf{r}_i), \quad i = 1, 2, \dots, N \quad (6)$$

The eigenvectors $\phi_1, \phi_2, \dots, \phi_N$ are called empirical orthogonal functions. Each ϕ_α is a 546-point (21×26 grid in this study) distribution of SST anomaly pattern. The eigenvalues, λ_α ($\alpha = 1, 2, \dots, N$), are all positive, and the summation of them, $\sum \lambda_\alpha$, equals the total variance. Therefore λ_α is considered as the portion of total variance “explained” by the EOF ϕ_α . It is convenient to label the eigenfunctions ϕ_α so that the eigenvalues are in descending order, that is,

$$\lambda_1 > \lambda_2 > \lambda_3 > \dots \quad (7)$$

The data matrix $\hat{T}(\mathbf{r}_n, \tilde{t}_p)$ is thus approximately written by

$$\hat{T}(\mathbf{r}_n, \tilde{t}_p) = \sum_{\alpha} PC_{\alpha}(\tilde{t}_p) \phi_{\alpha}(\mathbf{r}_n) \quad (8)$$

where $PC_{\alpha}(\tilde{t}_p)$ is the principal component with a unit of $^{\circ}\text{C}$ and a size of P , representing the temporal variation of the associated spatial pattern described by EOF $\phi_{\alpha}(\mathbf{r}_j)$.

4.2. Principal EOF Modes

Spatial and temporal variabilities can be quantitatively investigated with the method of EOF analysis and a number of its generalized forms. In order to delineate the major modes of 13 years (1981–1993), we perform a conventional EOF analysis and obtain the first six leading EOFs, which are able to account for

Table 1. Variances of the First Six Leading EOFs

EOF	Variance	Cumulative Variance
1	0.470	0.470
2	0.140	0.610
3	0.093	0.703
4	0.058	0.761
5	0.024	0.785
6	0.017	0.802

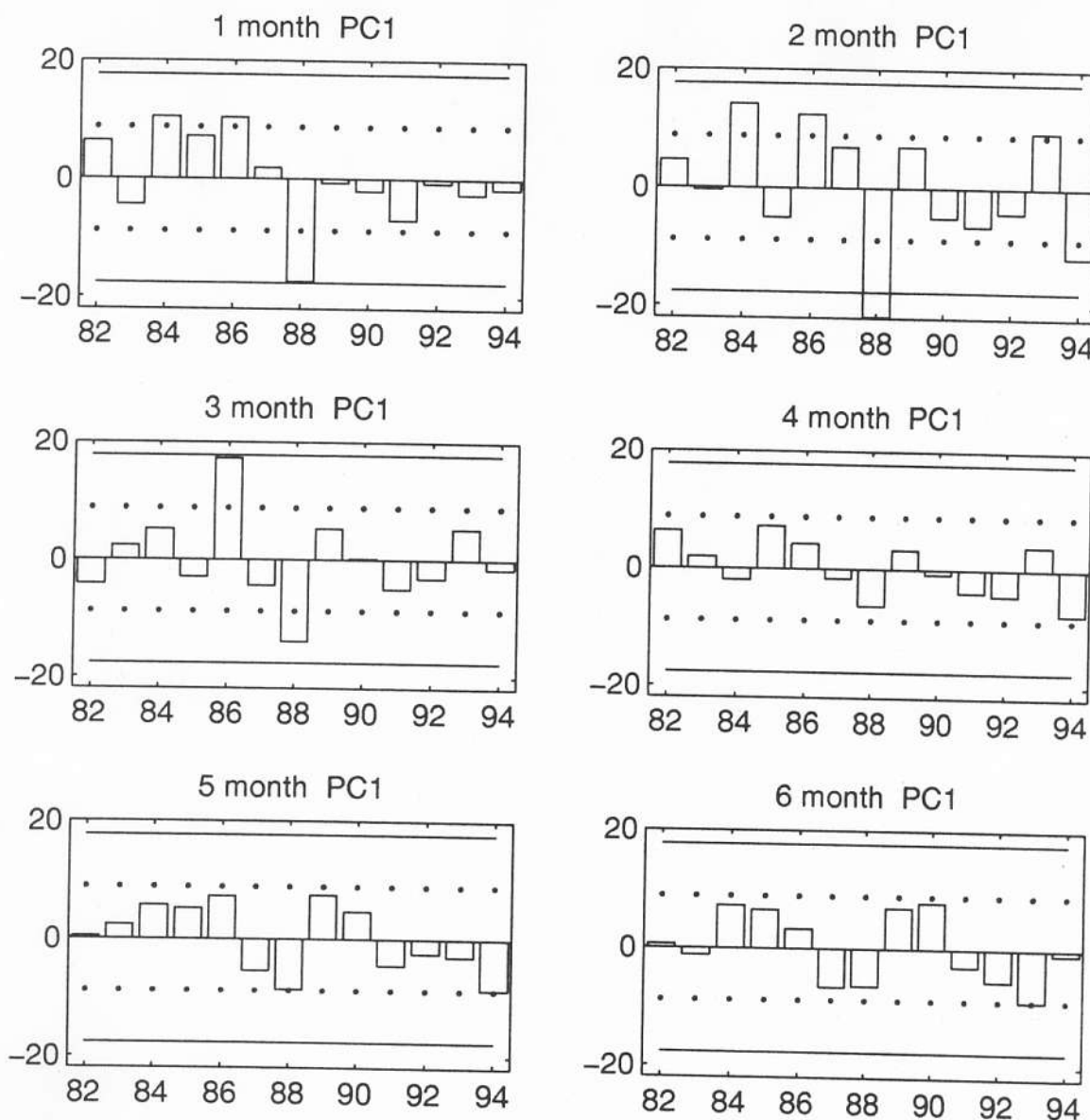


Figure 8. Time series of PC1 for 1982–1994. Here two solid lines are $PC_1 = 16.67$ and $PC_1 = -16.67$, and two dotted lines are $PC_1 = 8.83$ and $PC_1 = -8.83$.

almost 80.1% of the total variance during the seasons (Table 1). When combined, EOF1 and EOF2 explain over half (61%) of the total variance. Each EOF mode is normalized so that its total spatial variance is equal to unity. The patterns of the first six EOFs are deemed adequate to explain the SCS SST spatial variabilities (Figure 7).

The EOF1 mode (Figure 7a) shows a large warm/cool anomaly feature in the northern SCS (north of 12°N), which may reflect some nonseasonal process. The negative values of EOF1 indicate a northern SCS warm anomaly if $PC_1 < 0$ and a northern SCS cool anomaly if $PC_1 > 0$. Thus, we call EOF1 the northern SCS warm/cool anomaly mode.

The EOF2 mode (Figure 7b) shows a strong north-to-south contrast across the SCS, which probably reflects the interannual fluctuation of monsoons. If PC_2 is pos-

itive, the EOF2 mode shows a decrease of SST with latitude. If PC_2 is negative, the EOF2 mode shows an increase of SST with latitude. We call EOF2 the north-south contrast mode.

4.3. Temporal Variabilities

Northern SCS warm/cool anomaly mode. The first principal component $PC_1(\tilde{t}_p)$ for 1982–1994 shows the temporal variability of the northern SCS warm/cool anomaly (Figure 8). Since the EOF1 mode $\phi_1(\mathbf{r}_n)$ is always negative throughout the whole SCS (Figure 7a), positive values of $PC_1(\tilde{t}_p)$ correspond to negative SST anomalies (north SCS cool anomaly) and negative values of $PC_1(\tilde{t}_p)$ correspond to positive SST anomalies (north SCS warm anomaly). We see interannual variabilities in PC_1 , over periods of 2 to 5

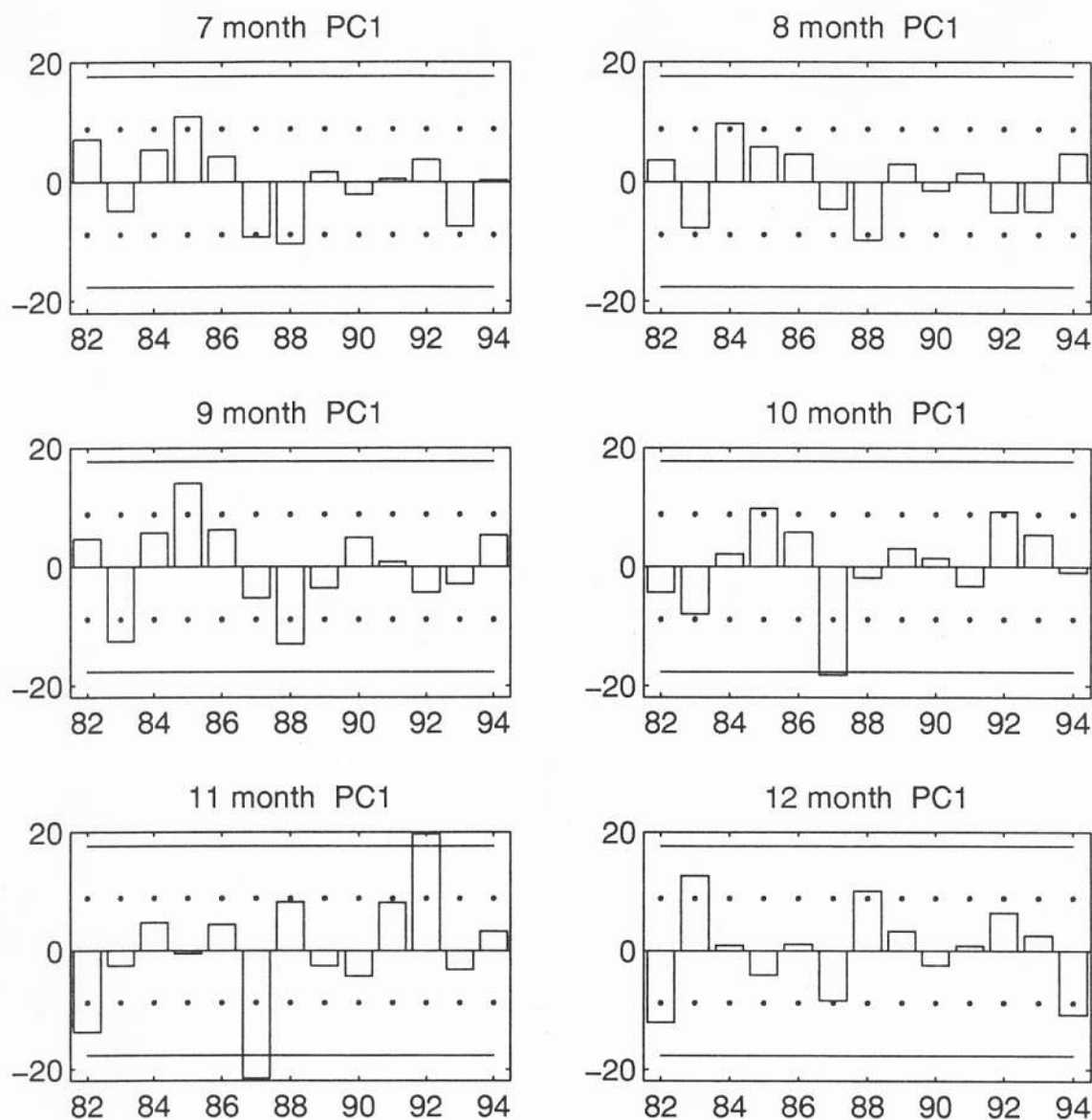


Figure 8. (continued)

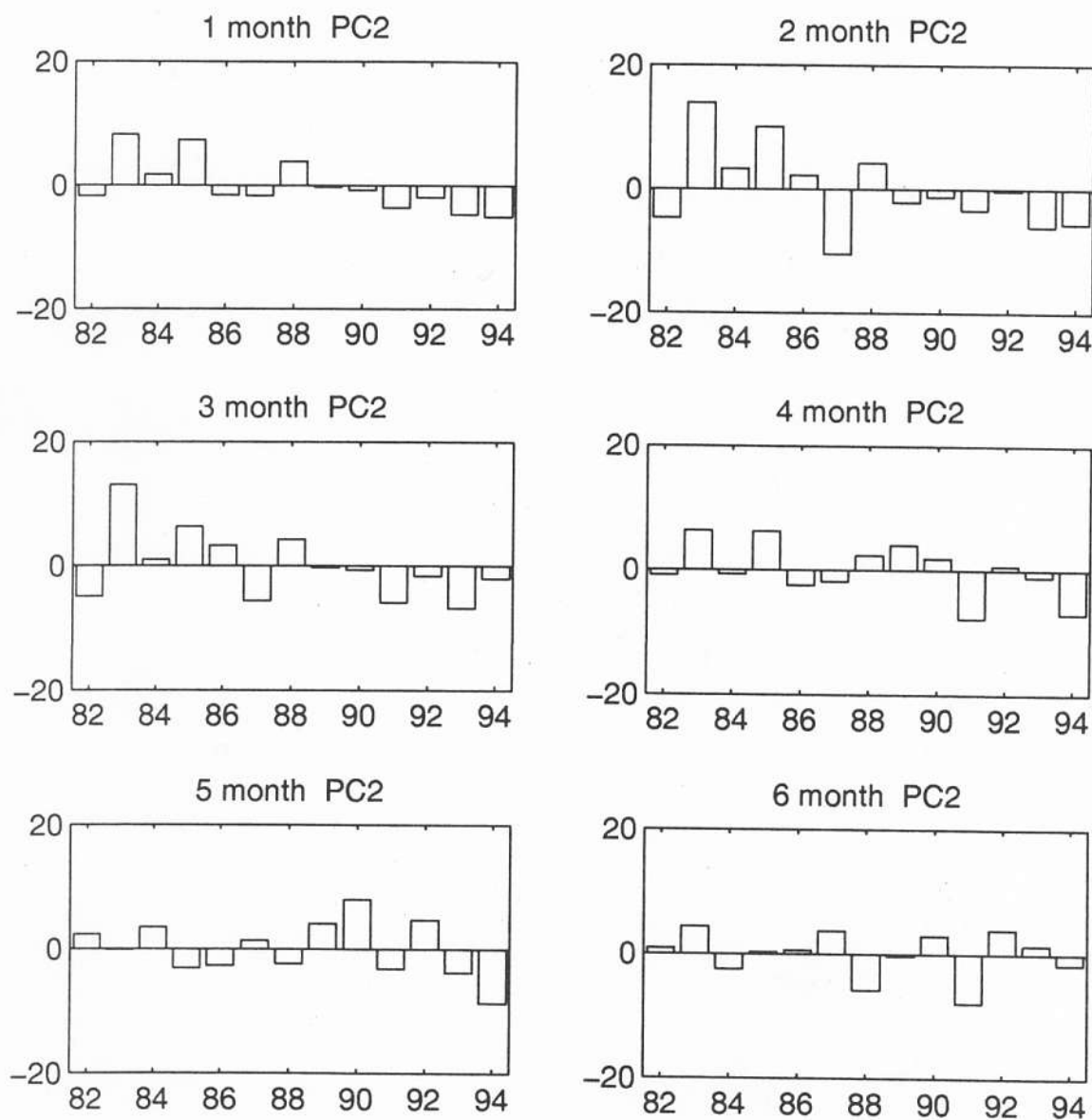
years. The maximum value of PC_1 is 20, appearing in November 1992, which indicates a strong northern SCS cool anomaly with mean monthly SST anomaly -1.2°C [$-20 \times (-0.06^\circ\text{C})$] in that month. The minimum value of PC_1 is -22, appearing in February 1988, which indicates a strong northern SCS warm anomaly with mean monthly SST anomaly 1.3°C [$-22 \times (-0.06^\circ\text{C})$] in that month. If the isoline of (-0.06°C) is treated as the boundary of the northern SCS warm/cool anomaly (Figure 7a), and if we are interested in evident warm/cool anomaly occurrence with SST anomaly exceeding 1°C , we found the following criteria: When $PC_1(\tilde{t}_p) \geq 16.67$, the northern SCS has a cool anomaly with transient SST anomaly of -1°C ; When $PC_1(\tilde{t}_p) \leq -16.67$, the northern SCS has a warm anomaly with transient SST anomaly of 1°C . If we consider a warm (or cool)

anomaly with transient SST anomaly of 0.5°C (or -0.5°C), the criterion becomes $PC_1(\tilde{t}_p) \geq 8.83$ (or $PC_1(\tilde{t}_p) \leq -8.83$). Four lines, $PC_1 = \pm 16.67$ (solid) and $PC_1 = \pm 8.83$ (dashed), were drawn in Figure 8 for identifying strong northern SCS transient SST anomalies. Table 2 lists the periods of strong ($|\Delta T| \geq 1^\circ\text{C}$) and evident ($|\Delta T| \geq 0.5^\circ\text{C}$) transient SST anomalies. We found two strong warm anomaly ($\Delta T \geq 1^\circ\text{C}$) periods (October–November 1987 and January–February 1988) and two strong cool anomaly ($\Delta T \leq -1^\circ\text{C}$) periods (March 1986 and November 1992).

North-south contrast mode. The second principal component $PC_2(\tilde{t})$ for 1982–1994 is shown in Figure 9. The EOF2 mode (Figure 7b) $\phi_2(\mathbf{r}_n)$, reveals the north-south contrast structure. Identification of the pattern (cool northern SCS and warm southern SCS or

Table 2. Northern SCS Warm and Cool Anomaly Periods

Anomaly Period	Above 1° C	Above 0.5° C
Warm	Oct.-Nov. 1987, Jan.-Feb. 1988	Jan.-Dec. 1982, Aug.-Oct. 1983 Jul. 1987 Oct. 1987-March 1988 May 1988, July-Sept. 1988 June-July 1993, Feb. 1994 April-May 1994, Dec. 1994
Cool	March 1986, Nov. 1992	Dec. 1983-Feb. 1984, Aug. 1984 July 1985, Sept.-Oct. 1985 Jan.-March 1986 Nov.-Dec. 1988 Nov. 1991 Oct.-Nov. 1992 Feb. 1993

**Figure 9.** The same as Figure 8 except for PC2.

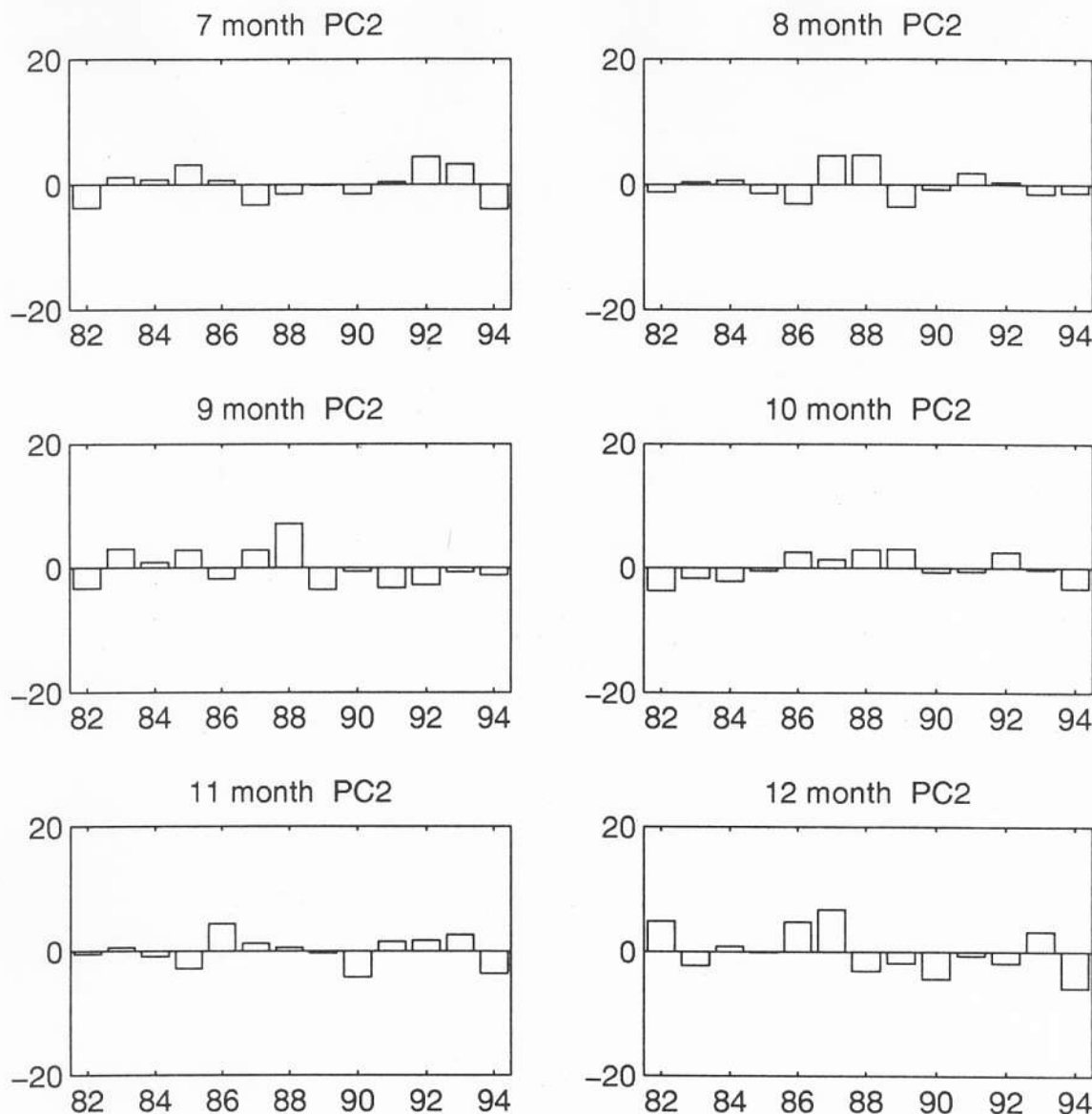


Figure 9. (continued)

vice versa) depends on the sign of $PC_2(\tilde{t})$. $PC_2(\tilde{t}) > 0$ corresponds to the decrease of SST with latitude pattern, and $PC_2(\tilde{t}) < 0$ corresponds to the increase of SST with latitude pattern. The maximum absolute value of PC_2 is 13, appearing in February 1983, which indicates a near 2°C south-to-north decrease of SST. The minimum value of PC_2 is -11, appearing in February 1987, which indicates a near 1.7°C north-to-south decrease of SST.

5. An Air-Sea Feedback Scenario

5.1. Cross Correlation Between ζ and T

We interpolated the wind stress curl (ζ) data ($2.5^\circ \times 2.5^\circ$) into the SST grid ($1^\circ \times 1^\circ$) and chose the period 1982-1989 for the cross correlation analysis. Cross correlation between ζ and T is computed at each grid point by

$$R_{\zeta, T}^{(\tau)}(x, y) = \frac{(t_N - 1)}{(t_N - |\tau|)} \times \frac{\sum_t \{ [\zeta(x, y, t) - \bar{\zeta}(x, y)] [T(x, y, t + \tau) - \bar{T}(x, y)] \}}{\sqrt{\sum_t [\zeta(x, y, t) - \bar{\zeta}(x, y)]^2} \sqrt{\sum_t [T(x, y, t) - \bar{T}(x, y)]^2}} \quad (9)$$

Here $t_N = 96$, the total months of the data sets. When $\tau > 0$, (9) represents correlation between τ months' leading of wind stress curl anomaly to SST anomaly, and $\tau < 0$ denotes correlation between $|\tau|$ months' leading of SST anomaly to wind stress curl anomaly.

5.2. Two Types of Cross-Correlation Coefficients

The no-lag cross correlation coefficient (CCC) between ζ and T (Figure 10) shows (1) negative CCC in

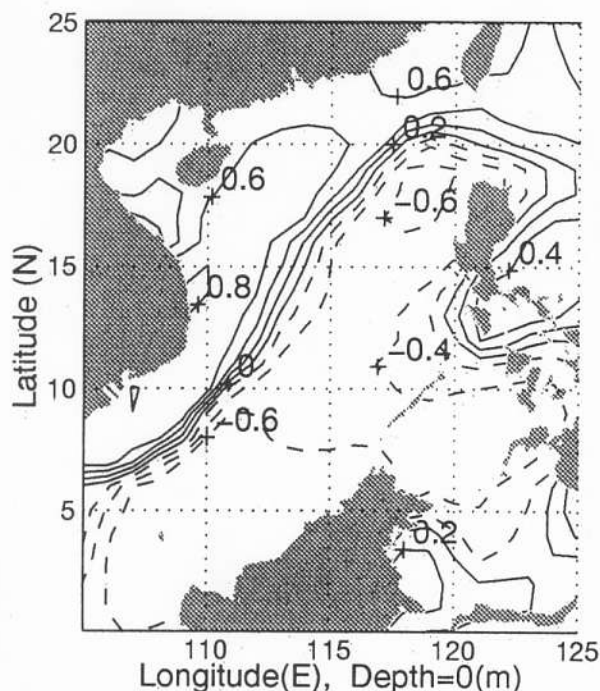


Figure 10. No lag cross-correlation coefficient between the surface wind stress curl and SST anomalies.

the deep basin of SCS (-0.6, minimum) and (2) positive CCC in the shelf regions of SCS (0.6, maximum). This basin negative - shelf positive (Bn-Sp) pattern continues as T lags ζ (oceanic response to the atmosphere) from 1 to 3 months (Figures 11a-11c). Both positive and

negative $R_{\zeta,T}^{(\tau)}$ strengthens when the lag begins. $R_{\zeta,T}^{(\tau)}$ has a minimum value of -0.7 and a maximum value of 0.8 as T lags ζ for 1 month (Figure 11a). As τ further increases ($\tau \geq 2$ months), both positive and negative $R_{\zeta,T}^{(\tau)}$ weakens (Figures 11c and 11d). When T lags ζ for 5 or more months (Figures 11f and 11g), $R_{\zeta,T}^{(\tau)}$ tends to have an out-of-phase pattern: basin positive - shelf negative (Bp-Sn) pattern.

As ζ lags T (atmospheric response to the ocean) for a month, the Bn-Sp pattern continues, but the CCC values are greatly reduced (Figure 12a). As $\tau = -2$ month, the Bn-Sp pattern disappears (Figure 12b). As $\tau = -3$ months (Figure 12c), the Bp-Sn pattern has been established and sustained for 4 months (Figures 12d-12f).

The dependence of CCC on τ (Figure 13) shows an oscillatory mode with a strong annual signal at 118°E , 18°N (in the SCS deep basin) and at 110°E , 14°N (in the Vietnam coast). For the deep basin point, CCC has a value of -0.6 at $\tau = 0$ (no time lag), decreases with τ to a minimum of -0.8 at $\tau = 1$ month (strongest negative correlation), and then increases with τ to a value near 0 at $\tau = 4$ months (no correlation). CCC increases from 0 to 0.8 (maximum) as the lag τ increases from 4 to 7 months and decreases again after $\tau = 7$ months. As τ decreases from 0 to -2 (ζ lags T from 0 to 2 months), CCC increases from -0.6 to 0 (no correlation). As τ decreases from -2 to -5 (ζ lags T from 2 to 5 months), CCC increases from 0 to 0.8 (strong positive correlation). The out-of-phase feature between the two

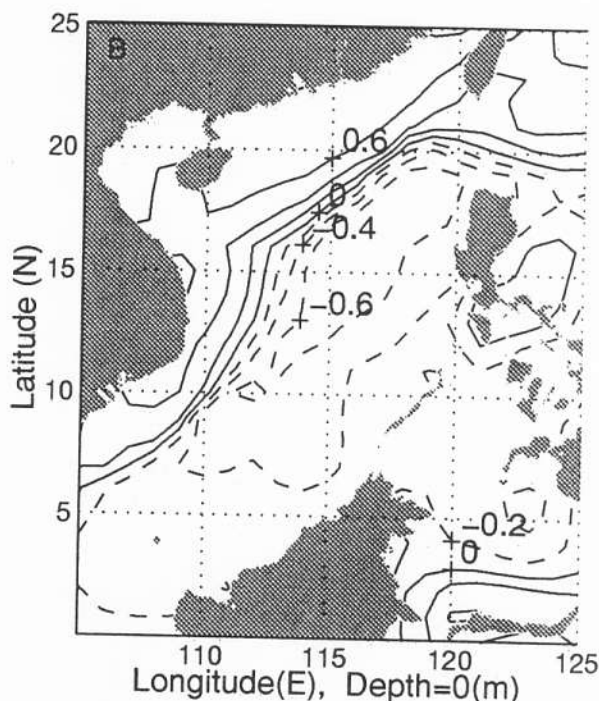
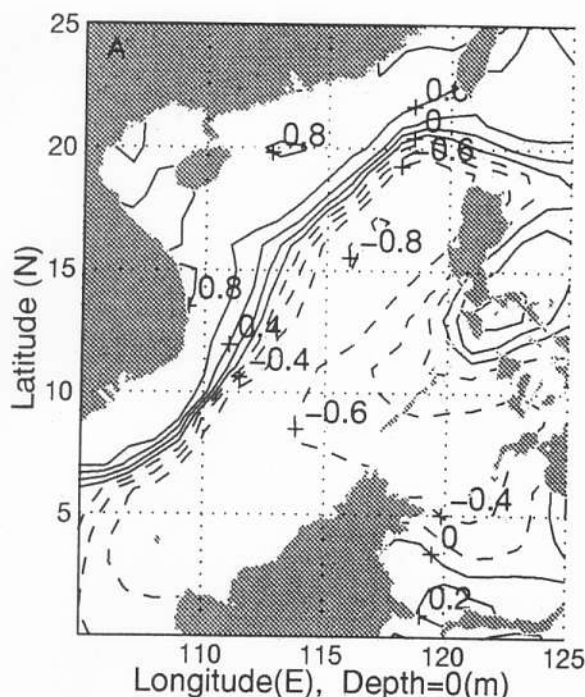


Figure 11. Cross-correlation coefficient between the surface wind stress curl and SST anomalies for various SST lags: (a) 1 month, (b) 2 months, (c) 3 months, (d) 4 months, (e) 5 months, and (f) 6 months.

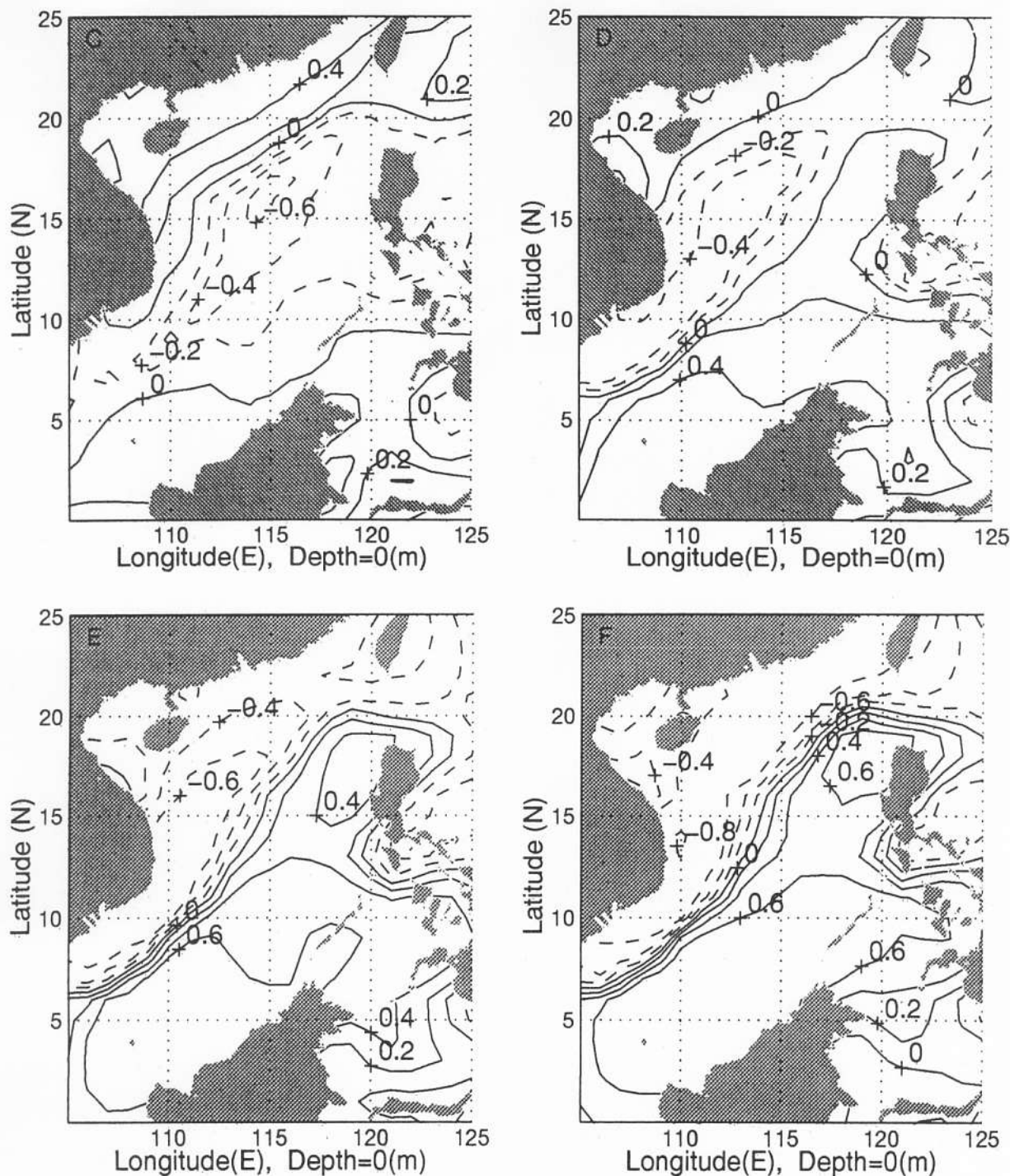


Figure 11. (continued)

regions (deep basin and shelf) indicates different physics to be involved in the air-sea feedback processes.

5.3. Possible Air-Sea Feedback Mechanism in the Northern SCS Basin

We may suggest an air-sea feedback mechanism in the SCS deep basin from the evident cross correlation between ζ and T for varying lag τ . The negative values of $R_{\zeta,T}^{(\tau)}$ ($0 \leq \tau \leq 3$) in the basin indicate the Ekman-

pumping effect: cyclonic wind stress curl induces upwelling which sucks the deep cold water to the surface, and anticyclonic wind stress curl generates downwelling which prevents the deep cold water to the surface. The cold (warm) SST anomaly tends to produce high (low) surface pressure perturbation which leads to the generation of anticyclonic (cyclonic) wind stress curl anomaly. Thus the values of $R_{\zeta,T}^{(\tau)}$ become positive in the basin as $-2 \geq \tau \geq -7$. The wind effect to generate the central SCS warm/cool SST anomalies has been verified

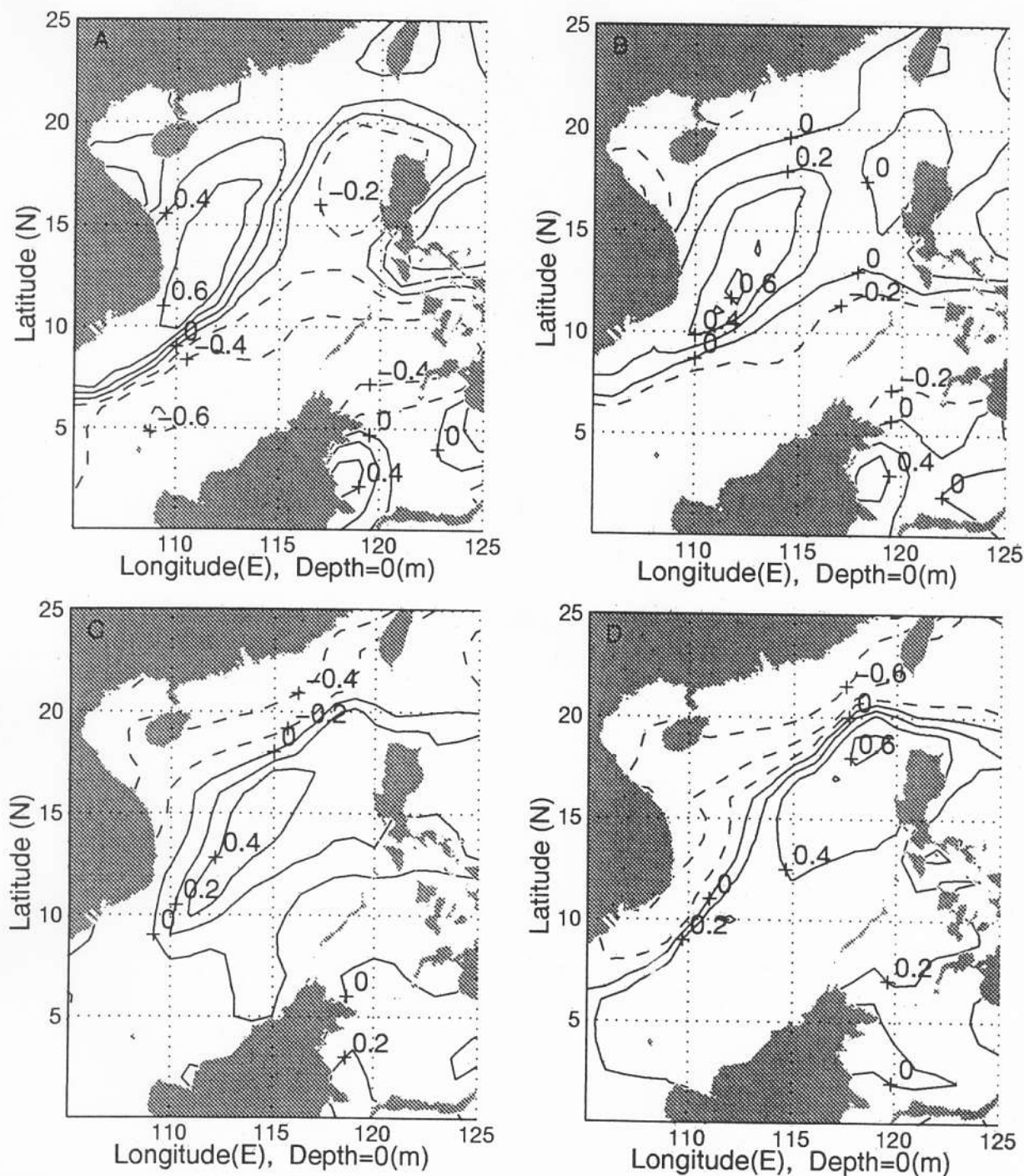


Figure 12. Cross-correlation coefficient between the surface wind stress curl and SST anomalies for various wind stress curl lags: (a) 1 month, (b) 2 months, (c) 3 months, (d) 4 months, (e) 5 months, and (f) 6 months.

by a numerical model (Chu et al., Generation of the South China Sea deep basin warm and cool anomalies by wind-topography forcing, submitted to *Journal of Geophysical Research*, 1997).

6. Conclusions

The goal of our study was to detect whether warm/cool anomaly exists in the SCS using the National Meteorological Center (NCEP) monthly sea surface temperature

(SST) fields (1982-1994). Composite and EOF analyses were used for the study. We obtained the following results from this observational study:

1. The ensemble mean SST field (\bar{T}) was established with a rather weak horizontal gradient (29°C near the Borneo coast to 26°C near the southeast China coast). This result agreed quite well with the early study using the Navy's Master Oceanographic Observation Data Set [Chu et al., 1996, 1997].

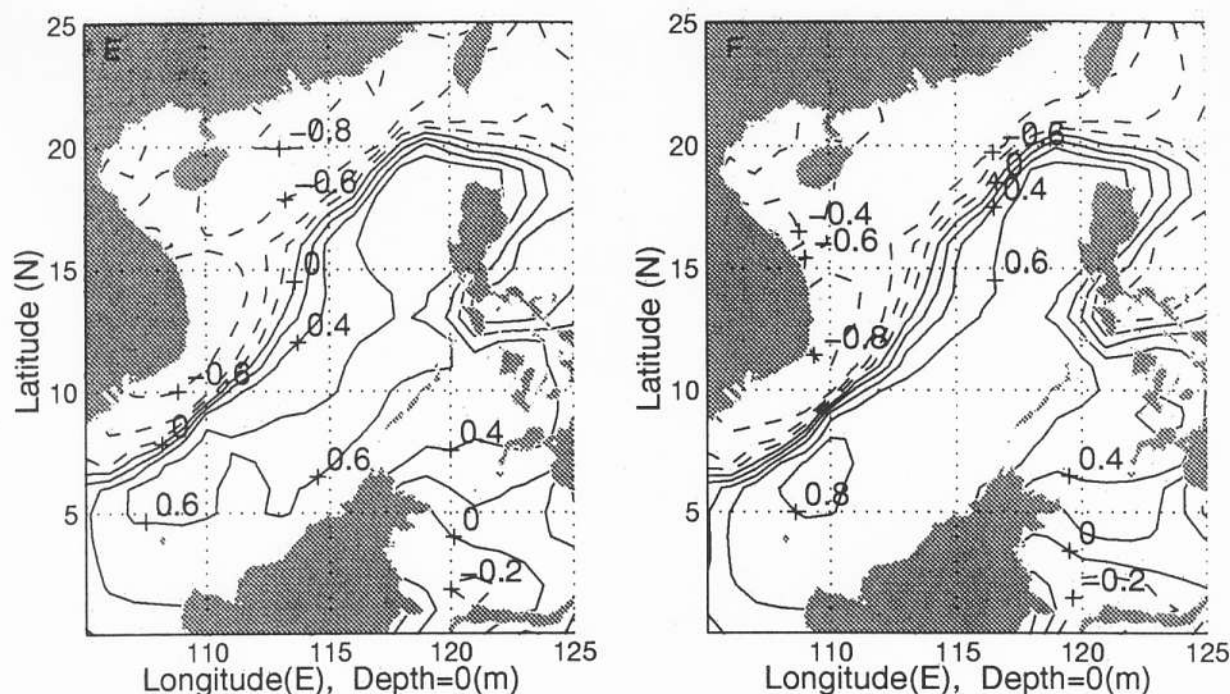


Figure 12. (continued)

2. The composite analysis indicates features of the monthly averaged SST anomaly fields relative to the ensemble mean. Four patterns, monsoon and transition each with two out-of-phase structures, were found. The monsoon pattern features northeast-to-southwest oriented isotherms in the northern SCS and a dipole

structure in the southern SCS. This thermal dipole is out-of-phase from winter to summer: The dipole with the WBP warm anomaly/SVC cool anomaly is found in winter and with the WBP cool anomaly/SVC warm anomaly in summer. The southern SCS dipole features a WBP warm anomaly ($\bar{T} > -1.2^{\circ}\text{C}$ in January)

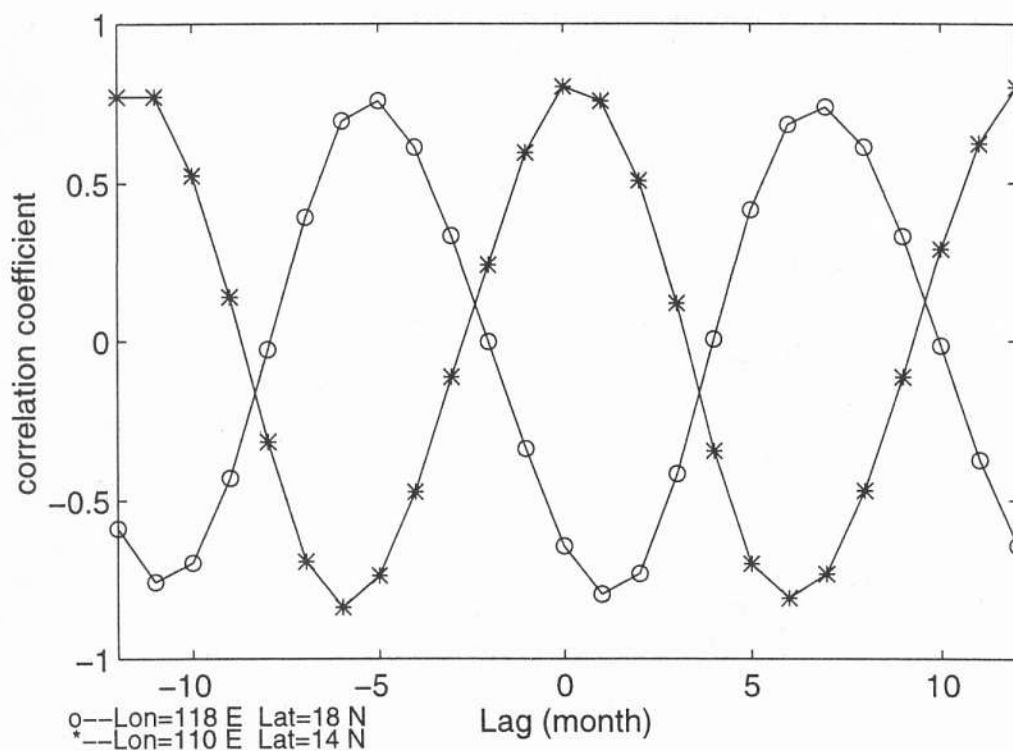


Figure 13. Cross-correlation coefficient between the surface wind stress curl and SST anomalies for various lags at 118°E , 18°N (circles, in the central SCS deep basin) and 110°E , 14°N (asterisks, in the Vietnam shelf).

and a SVC cool anomaly ($\tilde{T} < -2.4^{\circ}\text{C}$ in January) in winter (December to February); and a WBP cool anomaly ($\tilde{T} < 0.4^{\circ}\text{C}$ in July) and a SVC warm anomaly ($\tilde{T} > 1.0^{\circ}\text{C}$ in July) in the summer (June to September).

The transition pattern is characterized by the westward expansion of the WBP warm (cool) anomaly and the formation of the SCS warm (cool) anomaly in the spring-to-summer (fall-to-winter) transition. During the spring-to-summer transition (March to May), the warm anomaly is formed in the northern SCS with $\tilde{T} > 1.8^{\circ}\text{C}$ located at $112^{\circ}\text{--}119^{\circ}30'\text{E}$, $15^{\circ}\text{--}19^{\circ}30'\text{N}$. During the fall-to-winter transition (October to November), the northern SCS (north of 12°N) cool anomaly is formed in November with $\tilde{T} < -0.6^{\circ}\text{C}$ located at $108^{\circ}\text{--}115^{\circ}\text{E}$, $13^{\circ}\text{--}20^{\circ}\text{N}$.

3. Four patterns, monsoon and transition each with two out-of-phase structures, were found in the surface wind stress curl. The monsoon features a northwest anticyclonic (cyclonic) pattern and a southeast cyclonic (anticyclonic) pattern in winter (summer). The transition pattern features a southern SCS cyclonic/anticyclonic dipole. We found associations between the cyclonic (anticyclonic) wind stress curl and the warm (cool) anomaly with a seasonal phase shift. For the southern SCS, the fall-to-winter (spring-to-summer) ζ dipole pattern corresponds well with the winter (summer) \tilde{T} dipole pattern. For the central SCS, the winter (summer) ζ pattern corresponds well with the spring (fall) \tilde{T} pattern. We may claim that the winter (summer) ζ pattern causes the northward expansion of SVC warm (cool) anomaly in the spring (fall).

4. EOF analysis was applied to the residual SST data (relative to $\bar{T} + \tilde{T}$) to investigate the transient and interannual SST variabilities. EOF1 accounts for 47% of the variance and shows the northern SCS warm/cool anomaly pattern. The strongest northern SCS cool anomaly appears in November 1992 with mean monthly SST anomaly -1.2°C , and the strongest northern SCS warm anomaly shows up with mean monthly SST anomaly 1.3°C in November 1987 and February 1988. We also found two strong warm anomaly ($\Delta T \geq 1^{\circ}\text{C}$) periods (October–November 1987 and January–February 1988), and two strong cool anomaly ($\Delta T \leq -1^{\circ}\text{C}$) periods (March 1986 and November 1992).

5. An air-sea feedback mechanism was proposed from the cross correlation analysis between ζ and T . We will use a coupled air-sea model to verify this hypothesis.

Acknowledgments. NCEP reanalysis data provided through the NOAA Climate Diagnostics Center. We deeply thank Joe Metzger of the Naval Research Laboratory at Stennis Space Center and an anonymous reviewer for their critiques, which significantly improved this paper. This work was funded by the Naval Oceanographic Office, the Office of Naval Research NOMP and PO Programs, and the Naval Postgraduate School.

References

- Chu, P.C. and C.P. Chang, A case study of the South China Sea warm anomaly, paper presented at International CLIVAR-GOALS Workshop on Asian-Australian Monsoon Oceanography and Meteorology, World Meteorological Organization, Melbourne, Australia, April 10–12, 1995a.
- Chu, P.C. and C.P. Chang, South China Sea warm pool and monsoon development, paper presented at International South China Sea Monsoon Experiment (SCSMEX) Scientific Workshop, Chinese Meteorological Administration, Beijing, China, June 5–7, 1995b.
- Chu, P.C., and C.P. Chang, South China Sea warm pool in boreal spring, *Adv. Atmos. Sci.*, **14**, 195–206, 1997.
- Chu, P.C., H.C. Tseng, and C.P. Chang, South China Sea warm-core and cold-core eddies detected from the Navy's Master Oceanographic Observational Data Set, in *Proceedings on the Eighth Conference on Air-Sea Interaction*, pp. 176–180, Am. Meteorol. Soc., Boston, Mass., 1996.
- Chu, P.C., H.C. Tseng, C.P. Chang, and J.M. Chen, South China Sea warm pool detected in spring from the Navy's Master Oceanographic Observational Data Set (MOODS), *J. Geophys. Res.*, **15**, 761–15,771, 1997.
- Dale, W.L., Winds and drift currents in the South China Sea, *Malayan J. Trop. Geogr.*, **8**, 1–31, 1956.
- Hotelling, H., Analysis of a complex of statistical variables into principal components, *J. Educ. Psych.*, **24**, 417–441, 1933.
- Nitani, H., Oceanographic conditions in the sea east of Philippines and Lozon Strait in summer of 1965 and 1966, in *The Kuroshio-A Symposium on Japan Current*, edited by J.D. Marr, pp. 213–232, East-West, Honolulu, Hawaii, 1970.
- Reynolds, R.W., A real-time global sea surface temperature analysis, *J. Clim.*, **1**, 75–86, 1988.
- Reynolds, R.W., and D.C. Marsico, An improved real-time global sea surface temperature analysis, *J. Clim.*, **6**, 114–119, 1993.
- Reynolds, R.W., and T.M. Smith, Improved global surface temperature analyses using optimum interpolation, *J. Clim.*, **7**, 929–948, 1994.
- Richman, M.B., Rotation of principal components, *J. Climatol.*, **6**, 193–235, 1986.
- Soong, Y.S., J.H. Hu, C.R. Ho, and P.P. Niiler, Cold-core eddy detected in South China Sea. *Eos Trans. AGU*, **76**, 345, 347, 1995.
- South China Sea Institute of Oceanology, Integrated Investigation Report on Sea Area of the South China Sea, Vol. 2, pp. 183–231, Science Press, New York, 1985.
- Trenberth, K.E., J.G. Olson, and W.G. Large, A global ocean wind stress climatology based on ECMWF analyses, *NCAR Tech. Note, NCAR/TN-338+STR*, 93 pp., 1989.
- Weare, B.C., A.R. Navato, and R.E. Newell, Empirical orthogonal analysis of Pacific sea surface temperature, *J. Phys. Oceanogr.*, **6**, 671–678, 1976.

Y. Chen, P. Chu, and S. Lu, Department of Oceanography, Naval Postgraduate School, Monterey, California. (e-mail: chu@nps.navy.mil)

(Received July 19, 1996; revised March 21, 1997; accepted March 31, 1997.)